Influence of the Soret effect on binary-species boundary layers at high pressure

Takahiko Toki*
California Institute of Technology, Pasadena, CA, 91125, USA

Josette Bellan†
California Institute of Technology, Pasadena, CA 91125, USA
Jet Propulsion Laboratory, California Institute of Technology, Pasadena, CA 91109, USA

Direct numerical simulations of binary-species temporal boundary layers at high pressure are performed. The main objective is to investigate the influence of the Soret effect on flow physics of binary-species boundary layers where the fluid has a uniform composition. The working fluid is a mixture of 25% methane and 75 % nitrogen in mass fraction. Although the fluid composition is uniform at the initial condition, the mass fraction of methane increases near the wall when the wall temperature is hotter than the free stream temperature, whereas it decreases when the wall temperature is colder. The non-uniform mass fraction indicates that the uphill diffusion occurs near the wall. Investigation of fluctuations of the mass fraction reveals that the mass fraction fluctuates in the whole boundary layer, indicating that the uphill diffusion occurs even far from the wall. Examination of the species-mass diffusion balance for mean flow fields clarified that the Soret effect flux becomes large near the wall, and the large flux causes the non-uniform profile of the mass fraction near the wall.

I. Introduction

In many propulsion systems such as diesel engines, gas turbine engines, and rocket engines, the wall of the combustion chamber is exposed to a flow containing many species. Thus, the study of high-pressure multi-species boundary layers is a topic of wide interest. In those engines, the pressure is above critical pressures for several species of the mixture, and sometimes it may even be above the critical pressure for the fluid species mixture. For example, in aircraft, fuel combustion provides the energy and power to propel the aircraft; however, the fuel dispenses more energy that is used for propulsion purposes. Some of the heat released is transformed into useful power, however, the remaining heat must be dissipated or absorbed by other processes, so that it is not destructive to the engine. In a typical aircraft, approximately half of the heat is exhausted, and the other half must be appropriately mitigated so that it does not damage the aircraft structural components. Fuel is a convenient heat sink for several reasons. First, a large quantity of fuel is available and must be carried on the aircraft for operation purposes. Heating fuel prior to it entering the engine combustor is advantageous to the engine efficiency, but thermal stability of conventional jet fuel provides some limits. If fuel thermal limits are exceeded, fuel can degrade by oxidizing reactions or pyrolysis. As a result, viscous deposits can form in the fuel lines. Such deposits can foul the heat transfer surfaces, leading to decreased heat transfer performance and/or decreased engine performance [1]. Second, fuel is a liquid with good heat transfer properties. Thus, fuel is often used to cool pipes during aircraft operation thereby not only accomplishing the heat management goal, but also advantageously heating the fuel prior to entering the combustion chamber. Control and optimization of this cooling process is still an active topic of research and success in this endeavor could impact both military and commercial aircraft as well as address the formation of deposits on the pipe walls and impact durability. It is thus clear that in the above described situations, high-pressure multi-species boundary layer are the site large temperature gradients in the wall-normal direction due to the high temperature difference between wall and fluid. What makes the study of these boundary layers different from those involving a single chemical species [2] is that, as recently explained [3], the Soret effect, which becomes more prominent at high pressures, plays a significant role in determining the chemical composition. Therefore, the large temperature gradient may significantly influence flow physics in the multi-species boundary layer at high-pressure.

*Post-Doctoral Research Scholar, Department of Mechanical and Civil Engineering, 1200 E. California Blvd., Member AIAA
†Senior Research Scientist, 4800 Oak Grove Drive, AIAA Fellow

To investigate the flow physics of boundary layers at high pressure condition, several direct numerical simulations (DNS) have been performed. For example, Bae, Yoo & Choi[4] and Bae, Yoo & McEligot[5] simulated heated CO_2 turbulent vertical pipe and annular flows with buoyancy effects at small Mach numbers. They discovered that buoyancy effects cause M-shaped velocity profile and the unique velocity profile induces reduction of turbulent heat fluxes. Nemati et al.[6, 7] and Peeters et al.[8] also simulated vertical pipe and annular flows at small Mach numbers. The results from those investigations revealed that variations in dynamic viscosity and density significantly affect turbulent statistics and turbulent structure. While the previous studies relied on the low Mach number assumption, Kawai[2] simulated heated boundary layers of supercritical hydrogen over zero-pressure-gradient flat plates using a fully compressible DNS. He reported that real fluid effects at transcritical conditions induce strong density fluctuations and alter the Reynolds shear stress profile. Ma et al[9] studied a planar turbulent channel flow of supercritical nitrogen and demonstrated that semilocal scaling works reasonably well near the cooled wall, whereas the same scaling has limited success near the hot wall where violent fluctuations are found. Toki et al[10] also simulated a planar turbulent channel flow of supercritical nitrogen and introduced a new transform equation for a temperature profile in the logarithmic region. Kim et al.[11] simulated transcritical channel flow of R-134a and reported that even the recent improvements to the scaling laws cannot accurately capture the velocity distribution in the transcritical flow.

These DNS studies have mainly focused on effects of variations in thermodynamic properties and molecular transport properties in single-species boundary layers at high-pressure conditions, whereas the authors' knowledge there is a single study that investigated boundary layers composed of more than one species [3]. To fill the gap in understanding high-pressure multi-species boundary layers, Toki and Bellan [3] performed DNS of a temporal turbulent boundary layer of a mixture of nitrogen and methane. That study revealed that the Soret effect, which is also called thermophoresis, becomes occasionally larger in magnitude than the molecular diffusion flux near the wall. As a result, the study revealed that the Soret effect induces uphill diffusion in binary-species boundary layers at high pressure. However, the previous study only simulated cases in which the wall temperature is colder than free stream temperature, and thus the influence of the Soret effect with the hotter wall case is still unknown. In addition, in the previous study, a mass fraction gradient was imposed in the wall-normal direction and thus the influence of the Soret effect on a boundary layer having an initially uniform fluid mixture remains unknown.

In this study, DNS of binary-species boundary layers at high-pressure conditions is performed to investigate the influence of the Soret effect on flow physics of binary-species boundary layers where the fluid is initially a uniform mixture. Both hot and cold wall cases are simulated and the difference in outcome between these temperature conditions are highlighted. In §II, the governing equations consisting of the conservation equations and the equation of state are recalled. The numerical methods are briefly described in §III. The configuration, boundary conditions and initial conditions are summarized in §IV. The results are examined in §V, and we mainly discuss with the focus on mean profiles, turbulent fluctuations and species-mass diffusion balance. The findings from this study are summarized in §VI.

II. Governing equations

A. Differential conservation equations

The conservation equations for multi-species flow [12] are:

$$\frac{\partial \rho}{\partial t} + \frac{\partial}{\partial x_j}\left[\rho u_j\right] = 0, \tag{1}$$

$$\frac{\partial}{\partial t}\left(\rho u_i\right) + \frac{\partial}{\partial x_j}\left[\rho u_i u_j + p\delta_{ij} - \sigma_{ij}\right] = 0, \tag{2}$$

$$\frac{\partial}{\partial t}\left(\rho e_t\right) + \frac{\partial}{\partial x_j}\left[\left(\rho e_t + p\right) u_j - u_i\sigma_{ij} + q_j\right] = 0, \tag{3}$$

$$\frac{\partial}{\partial t}\left(\rho Y_\alpha\right) + \frac{\partial}{\partial x_j}\left[\rho Y_\alpha\, u_j + J_{\alpha j}\right] = 0, \tag{4}$$

where $\alpha \in [1, N-1]$, t denotes the time, x is a Cartesian coordinate, u is the velocity, $e_t = e + u_i u_i/2$ is the total energy (i.e. internal energy, e, plus kinetic energy), Y_α is the mass fraction of species α, N is the number of species, q is the heat flux and J_α is α-species mass flux. The Subscripts i and j refer to spatial coordinates, and we take x_1, x_2 and x_3 (or x, y and z) to mean the streamwise, wall-normal and spanwise directions. The Newtonian viscous stress tensor σ_{ij} is written as follows:

$$\sigma_{ij} = \mu\left(2S_{ij} - \frac{2}{3}S_{kk}\delta_{ij}\right), \quad S_{ij} = \frac{1}{2}\left(\frac{\partial u_i}{\partial x_j} + \frac{\partial u_j}{\partial x_i}\right), \tag{5}$$

where μ is the viscosity and S_{ij} is the strain-rate tensor.

Because of the different constitutive relations used for expressing J_α and q, equations (1) - (4) under high-pressure conditions have ultimately a different form from that used under atmospheric-pressure conditions. The present J_α and q expressions are based on the full matrices of mass-diffusion coefficients and thermal-diffusion factors derived by Harstad & Bellan [13]. In order to ensure global mass conservation, we consider a set of independent $(N-1)$ species equations rather than the set of N dependent species; in these $(N-1)$ equations, the original molar-fraction fluxes and the heat flux were rewritten to account for only $(N-1)$ gradients. The final form is

$$J_\alpha = -\rho\left[Y_\alpha\left(D_{T,\alpha}\right)\frac{\nabla T}{T} + Y_\alpha\left(D_{p,\alpha}\right)\frac{\nabla p}{p} + \sum_{\beta=1}^{N-1}\left(D'_{\alpha\beta}\frac{m_\alpha}{m_\beta}\right)\nabla Y_\beta\right], \tag{6}$$

$$q = -\lambda\nabla T + \sum_{\alpha=1}^{N-1}\mathbf{J}_\alpha\left[\left(\frac{h_\alpha}{m_\alpha} - \frac{h_N}{m_N}\right) - R_u T\left(\frac{\bar{\alpha}^b_{T,\alpha}}{m_\alpha} - \frac{\bar{\alpha}^b_{T,N}}{m_N}\right)\right] \tag{7}$$

where

$$D_{T,\alpha} = -\sum_{\beta=1}^{N}\bar{\alpha}^b_{T,\beta}\mathbb{D}_{\beta\alpha}, \qquad D_{p,\alpha} = \frac{p}{R_u T}\sum_{\beta=1}^{N} v_\beta\mathbb{D}_{\beta\alpha}, \tag{8}$$

$$D_{\alpha\gamma} = \sum_{\beta=1}^{N}\mathbb{D}_{\alpha\beta}\alpha_{D\beta\gamma}, \tag{9}$$

$$\bar{\alpha}^b_{T,\alpha} = \sum_{\beta=1}^{N} X_\beta\alpha^b_{T,\beta\alpha}, \tag{10}$$

$$D'_{\alpha\beta} = D_{\alpha\beta} - \left(1 - \frac{m_\beta}{m_N}\right)\left(\sum_{\gamma=1}^{N-1} D_{\alpha\gamma}X_\gamma\right). \tag{11}$$

Here, T is the temperature; $X_\alpha = Y_\alpha m/m_\alpha$ is the molar fraction; m_α is the species molar mass; m is the mixture molar mass, $m = \sum_{\gamma=1}^{N} m_\gamma X_\gamma$; $v_\alpha = (\partial v/\partial X_\alpha)_{T,p,X_\beta(\beta\neq\alpha)}$ is the partial molar volume, where the molar volume is $v = 1/n$ and $n = \rho/m$ is the molar density; $h_\alpha = (\partial h/\partial X_\alpha)_{T,p,X_\beta(\beta\neq\alpha)}$ is the partial molar enthalpy, where the molar enthalpy is $h = G - T(\partial G/\partial T)_{p,X}$ with G being the Gibbs energy; R_u is the universal gas constant; $D_{\alpha\gamma}$ are the pairwise mass diffusion coefficients; $\alpha^b_{T,\alpha\beta}$ are the binary thermal diffusion factors; and λ is the thermal conductivity. The mass-diffusion factors, $\alpha_{D\alpha\beta}$, are calculated from thermodynamics as

$$\alpha_{D\alpha\beta} \equiv \frac{1}{R_u T}X_\alpha\frac{\partial\mu_\alpha}{\partial X_\beta} = (\delta_{\alpha\beta} - \delta_{\alpha N}) + X_\alpha(R_{\alpha\beta} - R_{\alpha N}) \tag{12}$$

with $1 \leqslant \alpha \leqslant N,\ 1 \leqslant \beta \leqslant N-1$, and

$$R_{\alpha\beta} \equiv \frac{\partial \ln\gamma_\alpha}{\partial X_\beta} \tag{13}$$

with $1 \leqslant \alpha \leqslant N,\ 1 \leqslant \beta \leqslant N$. In equations (12) and (13), μ_α is the chemical potential of species α written in terms of $N-1$ species; $\gamma_\alpha \equiv \varphi_\alpha/\varphi^o_\alpha$ where φ is the fugacity coefficient written in terms of N species and the superscript o denotes the pure $(X_\alpha = 1)$ limit. Matrix elements $\mathbb{D}_{\beta\gamma}$ are the solution of the mixing rules equations[13]

$$\sum_{\beta=1}^{N}\left[\delta_{\alpha\beta} - \left(1 - \delta_{\alpha\beta}\right)X_\beta\frac{\bar{\mathcal{D}}_\alpha}{\mathcal{D}^b_{\alpha\beta}}\right]\frac{\mathbb{D}_{\beta\gamma}}{X_\beta} = \bar{\mathcal{D}}_\alpha\frac{\left(\delta_{\alpha\gamma} - Y_\alpha\right)}{X_\alpha} \tag{14}$$

where

$$\bar{\mathcal{D}}_\alpha = 1/\sum_{\substack{\beta=1\\ \beta\neq\alpha}}^{N}\left(\frac{X_\beta}{\mathcal{D}^b_{\alpha\beta}}\right). \tag{15}$$

Solutions for $\mathbb{D}_{\beta\gamma}$ may be obtained by an approximate inversion[14] as follows:

$$\mathbb{D}_{\beta\gamma} \simeq X_\beta \mathbb{D}^{(1)}_{\beta\gamma}, \tag{16}$$

$$\mathbb{D}^{(1)}_{\alpha\beta} = \frac{(1+Y_\alpha)}{X_\alpha}\mathcal{D}^*_\alpha \delta_{\alpha\beta} + \left(1-\delta_{\alpha\beta}\right)\frac{\mathcal{D}^*_\alpha \mathcal{D}^*_\beta}{\mathcal{D}^b_{\alpha\beta}} - \left(\sigma_\alpha \mathcal{D}^*_\alpha + \sigma_\beta \mathcal{D}^*_\beta\right) + \sum_{\gamma=1}^{N}\left(Y_\gamma \sigma_\gamma \mathcal{D}^*_\gamma\right), \tag{17}$$

$$\mathcal{D}^*_\alpha = (1-Y_\alpha)\,\bar{\mathcal{D}}_\alpha, \tag{18}$$

$$\sigma_\alpha = \frac{m_\alpha}{m}(1+Y_\alpha) + \sum_{\substack{\beta=1 \\ \beta\neq\alpha}}^{N} Y_\beta \frac{\mathcal{D}^*_\beta}{\mathcal{D}^b_{\alpha\beta}} \tag{19}$$

where $\mathcal{D}^b_{\alpha\beta}$ is the full approximation binary-diffusion matrix. This method leads to a singularity when the mixture is composed of only one species (as, for instance, in pure fuel zones). In that case equation (15) is no longer used and the diffusion coefficients are evaluated using the binary-diffusion matrix, by setting $\mathcal{D}^*_\alpha = \mathcal{D}^b_{\alpha N}$ where N represents the index associated with the solvent. This method was tested against an exact Gauss inversion (not shown) and it gave the same results, with an additional gain in computational time. Defining $\mathcal{D}_{\alpha\beta}$ as the first approximation of the binary diffusion matrix and realizing that the deviation of the ratio $\mathcal{D}^b_{\alpha\beta}/\mathcal{D}_{\alpha\beta}$ from unity is comparable to uncertainties in binary diffusion coefficients values[13], we assume $\mathcal{D}^b_{\alpha\beta} = \mathcal{D}_{\alpha\beta}$. The computation of $\mathcal{D}_{\alpha\beta}$ and $\alpha^b_{T,\alpha\beta}$ is described in references of [15] and [16].

B. Equation of state

Equations (1)-(4) are coupled with a modified Peng-Robinson (PR) equation of state (EOS)[17]

$$p = \frac{R_u T\left(\sum_{\alpha=1}^{\alpha=N} X_\alpha\right)}{(v_{PR} - b_{mix})} - \frac{a_{mix}}{\left(v^2_{PR} + 2b_{mix}v_{PR} - b^2_{mix}\right)} \tag{20}$$

where T and p are obtained as an iterative solution which satisfies both values of ρ and e, as obtained from the conservation equations . Here, v_{PR} is the molar PR volume, and $v = v_{PR} + v_s$ where v_s is the volume shift introduced for improving the accuracy of the PR EOS at high pressure, and the v_s computation was described in detail elsewhere in Ref. [18]. The values of a_{mix} and b_{mix} are written as follows:

$$a_{mix} = \sum_\alpha \sum_\gamma X_\alpha X_\gamma a_{\alpha\gamma}(T), \quad b_{mix} = \sum_\alpha X_\alpha b_\alpha, \tag{21}$$

where indices do not follow the Einstein notation, and

$$a_{\alpha\gamma} = (1-k'_{\alpha\gamma})\sqrt{\alpha_{\alpha\alpha}\alpha_{\gamma\gamma}}, \tag{22}$$

$$\alpha_{\alpha\alpha}(T) \equiv 0.457236(R_u T_{c,\alpha})^2 \times \frac{\left[1 + c_\alpha(1-\sqrt{T_{red,\alpha}})\right]^2}{p_{c,\alpha}},$$

$$c_\alpha = 0.37464 + 1.54226\Omega_\alpha - 0.26992\Omega^2_\alpha, \tag{23}$$

where $T_{red,\alpha} \equiv T/T_{c,\alpha}$, $T_{c,\alpha}$ is the critical temperature and Ω_α is the acentric factor. Also,

$$b_\alpha = 0.077796\frac{R_u T_{c,\alpha}}{p_{c,\alpha}}, \tag{24}$$

$$T_{c,\alpha\gamma} = \left(1-k_{\alpha\gamma}\right)\sqrt{T_{c,\alpha}T_{c,\gamma}} \ \text{ with } k_{\alpha\alpha} = 0, \tag{25}$$

$$v_{c,\alpha\gamma} = \frac{1}{8}\left(v^{1/3}_{c,\alpha} + v^{1/3}_{c,\gamma}\right)^3, \tag{26}$$

$$Z_{c,\alpha\gamma} = \frac{1}{2}\left(Z_{c,\alpha} + Z_{c,\gamma}\right), \tag{27}$$

Table 1 List of computational cases.

Case	Re_τ	δ_{99} (m)	u_w (m/s)	T_w (K)	T_∞ (K)	p_0 (atm)	$\frac{\rho_\infty}{\rho_w}$	$N_x \times N_y \times N_z$	$\mathcal{F}$
T300-600-CH4-25	492	0.063	155	300	600	60	0.47	$768 \times 384 \times 512$	2549
T600-300-CH4-25	494	0.052	215	600	300	60	2.12	$768 \times 512 \times 512$	1284

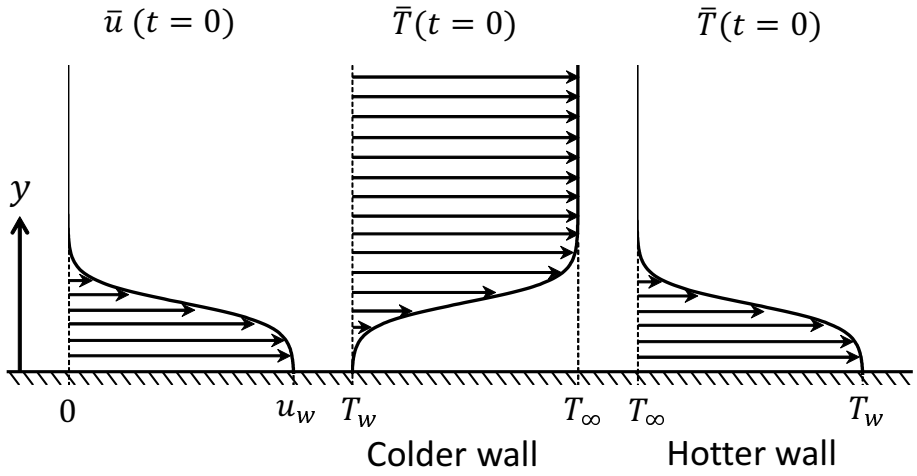

Fig. 1 Illustration showing initial profiles of streamwise velocity and temperature.

$$p_{c,\alpha\gamma} = \frac{R_u T_{c,\alpha\gamma} Z_{c,\alpha\gamma}}{v_{c,\alpha\gamma n}}, \tag{28}$$

with $T_{red,\alpha\gamma} \equiv T/T_{c,\alpha\gamma}, Z_{c,\alpha}$ being the critical compression factor with the compression factor defined as $Z = p/(\rho T R_u/m)$, $v_{c,\alpha}$ being the critical volume, and $p_{c,\alpha}$ being the critical pressure. $k_{\alpha\gamma}$ is an empirical mixing parameter. The relationship between parameters $k_{\alpha\gamma}$ and $k'_{\alpha\gamma}$ is

$$(1 - k_{\alpha\gamma}) = (1 - k'_{\alpha\gamma}) \frac{(v_{c,\alpha} v_{c,\gamma})^{1/2}}{v_{c,\alpha\gamma}}. \tag{29}$$

and $k'_{\alpha\gamma}$ is set to 0.0311 for the mixture of nitrogen and methane[19].

III. Numerical method

The differential equations combined with the equation of state described in §II were numerically solved using a fourth-order explicit Runge-Kutta time integration and a sixth-order compact scheme spatial discretization [20]. In order to ensure time stability, the conservative variables were filtered using the eighth-order compact filter described in Ref. [21]. A parametric study (not shown) using several filter coefficients (0.45, 0.475 and 0.49) indicated that the value 0.49 was sufficiently large to ensure that the filter only acts on the shortest wavelengths that can be resolved on the grid and it does not affect the physical content of the data. The code was parallelized using three-dimensional domain decomposition and message passing. The tridiagonal solvers for the compact derivative scheme and the compact filter were efficiently parallelized using the method of Ref. [22].

IV. Configuration, boundary conditions and initial conditions

The configuration is that of a temporal boundary layer. Figure 1 provides a sketch of the initial conditions. The wall is moving at constant velocity, while the far field remains at rest. The working fluid is a mixture of nitrogen and methane. Periodic boundary conditions are applied to the streamwise (x) and spanwise (z) directions. No-slip wall

Table 2 Grid resolution and maximum resolution using the Kolmogorov scale η_K.

Case	Δx^+	Δy_1^+	Δy_t^+	Δz^+	$(\Delta x/\eta_k)_{\max}$	$(\Delta y/\eta_k)_{\max}$	$(\Delta z/\eta_k)_{\max}$
T300-600-CH4-25	4.5	0.32	10.6	3.4	3.1	0.6	2.3
T600-300-CH4-25	5.4	0.29	9.6	4.0	3.9	1.5	2.9

conditions are applied at the wall, and the temperature and velocity are there constant in space and time. In the past, the same configuration was used to conduct DNS of an incompressible boundary layer by Kozul et al.[23], and it was shown that turbulent statistics of the temporal set-up agree very well to those of spatial boundary layers. Compared to the Ref. [23], the upper-domain boundary condition is different and specified to be non-reflecting [12], and the mass flux of each species is specified to be null at a wall. Two cases with different temperature conditions are simulated and they are summarized in table 1. For the simulation denoted as T300-600-CH4-25 the wall temperature is 300 K and the free stream temperature is 600 K and for the simulation labeled T600-300-CH4-25 the wall temperature is 600K and the free stream temperature is 300 K. The initial composition is uniform; the initial mass fraction of methane is 25% and that of nitrogen is 75% in both cases. In table 1, Re_τ is a friction Reynolds number, δ_{99} is 99% of boundary layer thickness, u_w is wall velocity, T_w is wall temperature, T_∞ is far field temperature, p_0 is initial pressure, ρ_∞/ρ_w is density ratio between the wall and the far field, N_x, N_y and N_z are numbers of grid points in each direction, and $\mathcal{F}$ is a viscosity scaling factor introduced so that DNS is possible at the Reynolds number value of the simulation; all transport properties are scaled by $\mathcal{F}$ to ensure that the Schmidt and Prandtl numbers have physical values. Details regarding $\mathcal{F}$ are discussed elsewhere [15, 16].

A. Initial velocity and temperature profiles

The initial velocity and temperature profiles are composed of mean quantities upon which perturbations are imposed. The mean profiles are based on the tangent hyperbolic function, and perturbations are analytically derived by stability analyses provided in Ref. [3]. The mean profiles are specified to resemble a shear layer as follows:

$$\overline{u}(y) = U_w - \frac{1}{2}U_w\left(1 - \tanh\left[\frac{D}{2\theta_{sl}}\left(1 - \frac{y}{D}\right)\right]\right) \tag{30}$$

$$\overline{T}(y) = T_w + \frac{1}{2}\left(T_\infty - T_w\right)\left(1 - \tanh\left[\frac{D}{2\theta_{sl}}\left(1 - \frac{y}{D}\right)\right]\right) \tag{31}$$

$$p = p_0, \quad v = 0, \quad w = 0 \tag{32}$$

where D is displacement thickness, and θ_{sl} is momentum thickness of the shear layer. The overline $\overline{(\cdot)}$ indicates averaging in the homogeneous (x, z) plane. The subscripts w and ∞ indicate wall and far field respectively. The Mach number of the wall velocity is 0.4 based on the sound speed of the mixture of 25% methane and 75% nitrogen. The displacement thickness D is set to $Re_D \equiv DU_w/\nu = 1000$, following Kozul et al.[23] who did a parametric study of the initial profile based on Re_D and demonstrated that in those cases $Re_D = 1000$ results in a natural turbulent evolution as soon as the computation was initiated. The momentum thickness θ_{sl} is determined by stability analyses in order to achieve the largest growth rate for the initial perturbations.

B. Domain size and grid spacing

The domain size is determined by the planed boundary layer thickness, δ_p corresponding to the value of Re_τ at which the data will be analyzed. For the simulations to be comparable to the spatial boundary layer of Schlatter & Örlü at $Re_\tau = 492$[24], the planned friction Reynolds number is 500. When the friction Reynolds number is 500, the boundary layer thickness is less than 0.07 m in the present cases. Thus, the planed boundary layer thickness is set to 0.07 m. The wall-normal domain size is set to $L_y = 3\delta_p$. The streamwise domain size is set to $L_x = 2\pi\delta_p$, and the spanwise domain size is set to $L_z = \pi\delta_p$. This domain size was proved to be sufficiently large to capture the main dynamic features of the flow and the wall-normal statistics [23]. Additionally, two-point correlations were computed in a previous study[3], that compared very favorably with similar plots in the literatures of [25, 26]. The grid spacing is uniform in streamwise and spanwise directions. The grid spacing in wall-normal direction is determined by the

following tangent hyperbolic function:

$$y_j = \frac{L_y}{\alpha_{st}} \tanh\left[-1 + \frac{j-1}{N_y - 1} \tanh^{-1}(\alpha_{st})\right] \tag{33}$$

where α_{st} is an constant value of $\alpha_{st} = 0.985$ and N_y is a number of grid points in wall-normal direction. The wall-normal coordinates based on wall units are defined as $y^+ \equiv y u_\tau / \nu_w$. The grid resolutions in wall units are shown in table 2. They are evaluated as $\Delta x_i^+ \equiv \Delta x_i u_\tau / \nu_w$, where Δx_i is the grid spacing in the x_i direction; Δx^+ and Δz^+ are grid resolutions in streamwise and spanwise directions, respectively. The wall-normal grid spacings Δy_t^+ and Δy_1^+ correspond to those at the top and bottom of the domain. In addition, table 2 lists the maximum grid spacing in terms of the Kolmogorov scale η_k calculated as

$$\eta_k = \left(\frac{(\overline{\mu})^3}{(\overline{\rho})^2 \varepsilon}\right)^{1/4}, \tag{34}$$

where $\varepsilon \equiv \overline{\sigma'_{ij} \partial u'_i / \partial x_j}$ is the turbulent kinetic energy dissipation. The notation $(\cdot)'$ indicates fluctuation about the mean. Prior DNS studies have reported the resolution requirements of $\Delta x < 12 \min\{\eta_k, \eta_\theta\}, \Delta y < 2 \min\{\eta_k, \eta_\theta\}, \Delta z <$

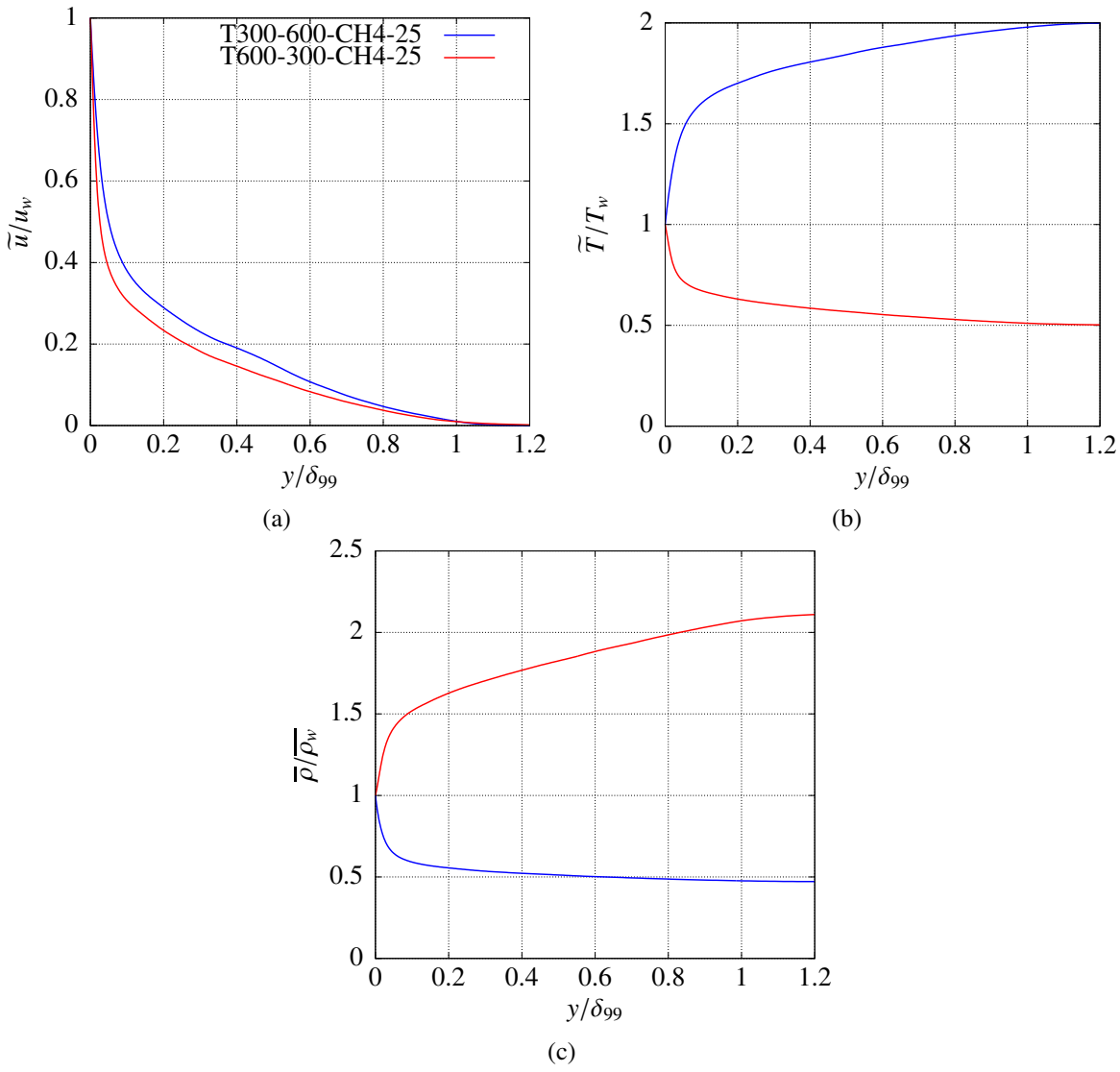

Fig. 2 Mean profiles of (a) streamwise velocity, (b) temperature and (c) density.

$6\min\{\eta_k, \eta_\theta\}$ where $\eta_\theta \equiv \eta_k\sqrt{1/Pr}$ is the Bachelor scale[2, 27–29]. Table 2 shows the current grid resolutions satisfy the requirements in terms of the Kolmogorov scale. Since the molecular Prandtl number Pr is less than 1 in all cases, the requirements about the Batchelor scale are also satisfied. However, these requirements are insufficient for binary-species flows, because the Soret effect and the species mass-diffusion can affect the length scale of thermal diffusion [15]. Therefore, we investigated one-dimensional spectra to check the grid resolutions (not shown). The spectra of all quantities show the smoothness associated with turbulent characteristics, and there is no accumulation at the smallest scales. Therefore, the present grids have excellent resolutions.

V. Results

The results are presented at $Re_\tau \simeq 500$.

A. Mean profiles

Figure 2 shows mean profiles of streamwise velocity, temperature and density. The tilde $\widetilde{(\cdot)}$ indicates Favre averaging in the homogeneous (x, z) plane. These mean profiles are nondimensionalized by values at the wall. The velocity monotonically decreases from the wall to the far field in both cases because the wall is moving and the far field is at rest in the present simulations. The gradient is steeper near the wall due to the suppression of turbulence at that location. The velocity profiles are similar in both cases. In contrast, since the imposed temperature conditions are different, the temperature profiles differ between the two cases. For T300-600-CH4-25 the temperature monotonically increases from the wall, whereas for T600-300-CH4-25 it monotonically decreases. However, in both cases the temperature gradient becomes steeper near the wall. As expected, the temperature difference affects the density profiles; for T300-600-CH4-25 the density monotonically decreases from the wall due to the temperature increase whereas for T600-300-CH4-25 the density monotonically increases from the wall.

Figure 3 shows profiles of mass fraction of methane as a function of either y/δ_{99} or y^+. Although the composition of the fluid is uniform at the initial condition, in both cases the mass fraction acquires non-uniformities in the wall-normal direction. For T300-600-CH4-25, the mass fraction of methane is 0.25 at the initial condition, and it appears that closer to the wall than $y^+ = 20$ the mass fraction decreases. In contrast, for T600-300-CH4-25 the mass fraction increases at locations closer to the wall than $y^+ = 20$. The analysis below focuses on explaining this result.

The relevant perspective involves considerations of mass diffusion. In the past, species-mass diffusion has been classified as either regular or uphill [16, 30]. Regular diffusion occurs when the flux is directed from regions of large

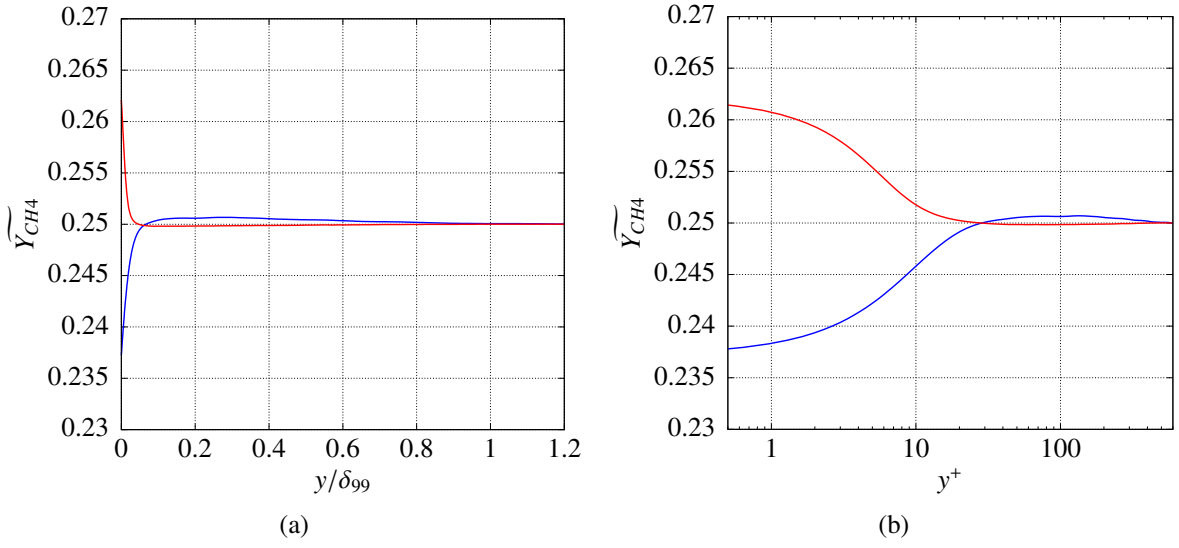

Fig. 3 Mean profiles of mass fraction of methane as a function of the outer scaling y/δ_{99} (a) and as a function of the wall unit y^+ (b). Line legend as in figure 2

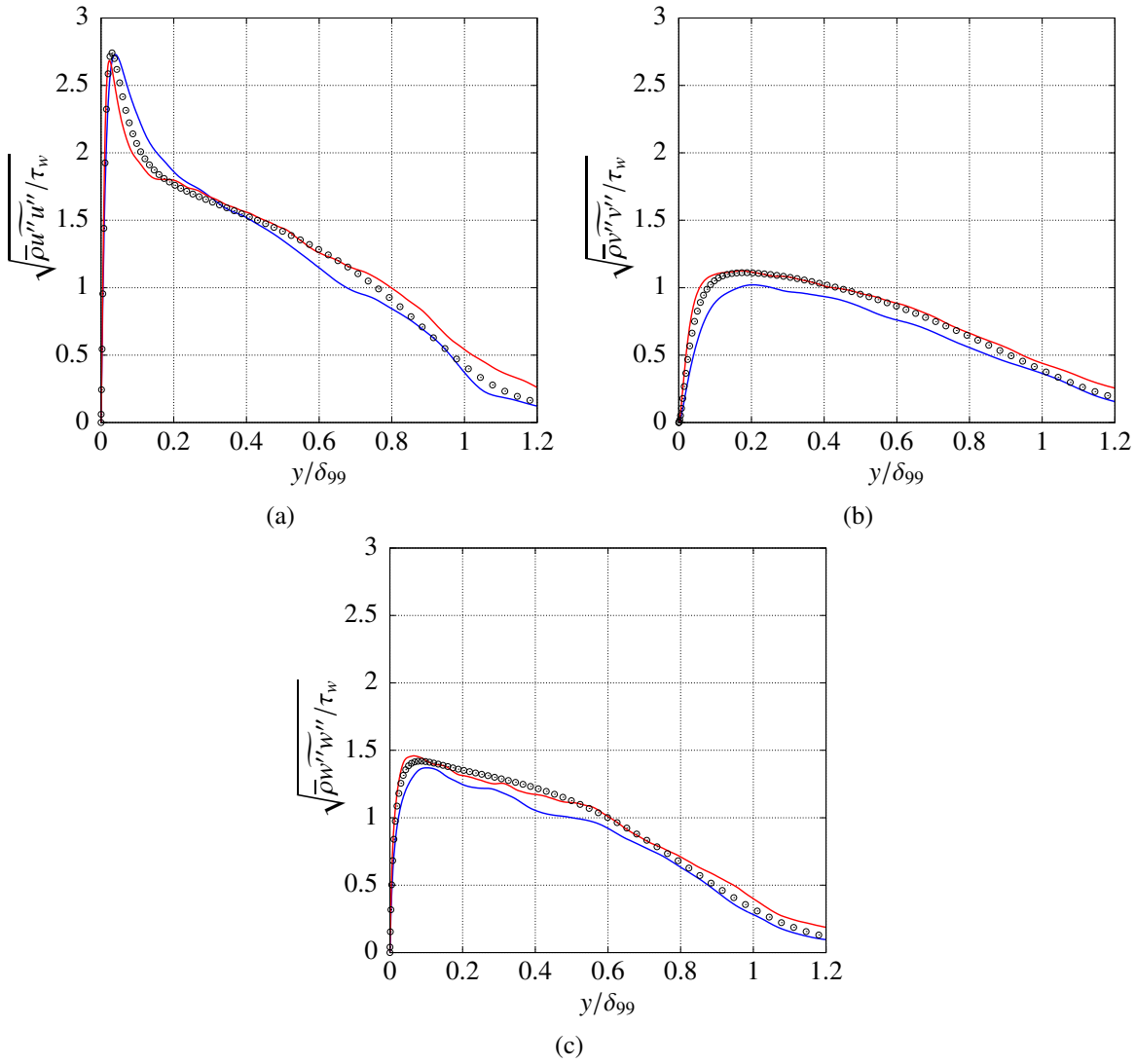

Fig. 4 Velocity fluctuations in (a) streamwise, (b) wall-normal and (c) spanwise directions. Line legend as in figure 2. Circles incompressible constant-property boundary layer by Schlatter et al.[24].

concentrations to regions of low concentration, while uphill diffusion occurs when the flux is directed from regions of low concentrations to regions of large concentration. In the present situation, if only regular diffusion would occur, the mass fraction would be invariant form the initial condition which is specified as a uniform composition. Thus, the variation in the mass fraction near the wall indicates that uphill diffusion occurs in the present simulations.

B. Turbulent fluctuations

To examine whether the effect of the uphill diffusion extends to turbulence, figure 4 shows velocity fluctuations. The notation $(\cdot)''$ indicates fluctuations about the Favre average and the fluctuations are nondimensionalized by the wall shear stress. The DNS data of the incompressible constant-property turbulent boundary layer at $Re_\tau = 492$ by Schlatter et al.[24] is also included in the figure. The fluctuation profiles of the present DNS are similar to those of the incompressible DNS data. This result indicates that the qualitative characteristics of momentum diffusion are the same as those of the incompressible flow. In addition, this result also indicates that the variation in the mass fraction due to the uphill diffusion does not significantly affect turbulent fluctuations.

Figure 5 depicts fluctuations of the methane mass fraction. The fluctuations are nondimensionalized by the mass fraction at each y location. The mass fraction fluctuations have a peak at approximately $y/\delta_w = 0.05$ for both simulations.

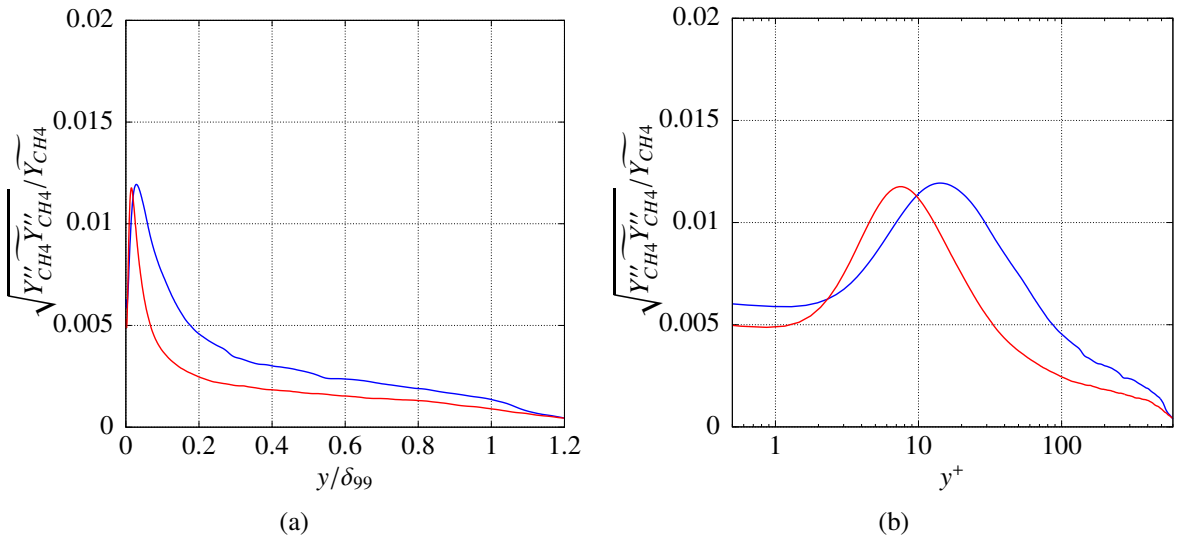

Fig. 5 Fluctuations of mass fraction of methaneas a function of the outer scaling y/δ_{99} (a) and as a function of the wall unit y^+ (b). Line legend as in figure 2.

If the fluid composition is uniform, the mass fraction should not fluctuate even in turbulent flows. Therefore, the fluctuations are also due to the uphill diffusion which renders the mass fraction nonuniform. In addition, although the gradient of mass fraction is almost null past $y^+ = 20$, the fluctuations do not decrease to 0 past $y^+ = 20$. This result indicates that the uphill diffusion occurs even far from the wall.

C. Species-mass diffusion balance in the mean flow field

The mean profile of the mass fraction of methane revealed that uphill diffusion occurs in the present configuration resulting in a mass fraction gradient. To elucidate the reason of the development of the species mass fraction gradient, the diffusion balance is investigated.

For the purpose of this analysis, equation (4) is averaged in the homogeneous (x, z) plane and since through averaging the derivatives in the homogeneous directions are null, the following equation holds:

$$\frac{\partial}{\partial t}\left(\overline{\rho}\widetilde{Y_\alpha}\right) + \frac{\partial}{\partial y}\left[\overline{\rho}\widetilde{Y_\alpha}\widetilde{v} + \overline{\rho}\widetilde{Y''_\alpha v''} - \overline{\rho Y_\alpha \left(D_{T,\alpha}\right)\frac{\partial T}{\partial y}} - \overline{\rho Y_\alpha \left(D_{p,\alpha}\right)\frac{\partial p}{\partial y}} - \sum_{\beta=1}^{N-1}\overline{\rho\left(D'_{\alpha\beta}\frac{m_\alpha}{m_\beta}\right)\frac{\partial Y_\beta}{\partial y}}\right] = 0. \tag{35}$$

Equation (35) shows that the α-species species-mass flux for the mean flow field is given by

$$J_{mean}(y) = \overline{\rho}\widetilde{Y_\alpha}\widetilde{v} + \overline{\rho}\widetilde{Y''_\alpha v''} - \overline{\rho Y_\alpha \left(D_{T,\alpha}\right)\frac{\partial T}{\partial y}} - \overline{\rho Y_\alpha \left(D_{p,\alpha}\right)\frac{\partial p}{\partial y}} - \sum_{\beta=1}^{N-1}\overline{\rho\left(D'_{\alpha\beta}\frac{m_\alpha}{m_\beta}\right)\frac{\partial Y_\beta}{\partial y}}, \tag{36}$$

where the first term is the mean flow flux, the second term is the turbulent flux, the third term is the Soret effect flux, the fourth term is the pressure gradient flux, and the fifth term is the molecular diffusion flux.

Figure 6 shows the profiles of these five terms for methane as a function of either y/δ_{99} or y^+. The mean flow flux in absolute value is large over $y^+ = 100$ in both cases, a fact which is traced to the temperature difference between the wall and the far field. For example, for T600-300-CH4-25 since the wall temperature is hotter than the fluid, the fluid receives heat from the wall. The heated fluid expands and the expansion causes an upward velocity in the wall-normal direction. The upward velocity causes the large mean flow flux. The opposite occurs in T300-600-CH4-25. However, the mean flow flux is small near the wall below $y^+ = 10$, and the Soret effect flux and the molecular diffusion flux become dominant. Since the variation in the mass fraction occurs only near the wall, this result indicates that the Soret effect and the molecular diffusion fluxes are related to this variation. The physics of the mass fraction gradient can be explained as follows. The mass fraction is uniform at the initial condition, but the temperature has a gradient because

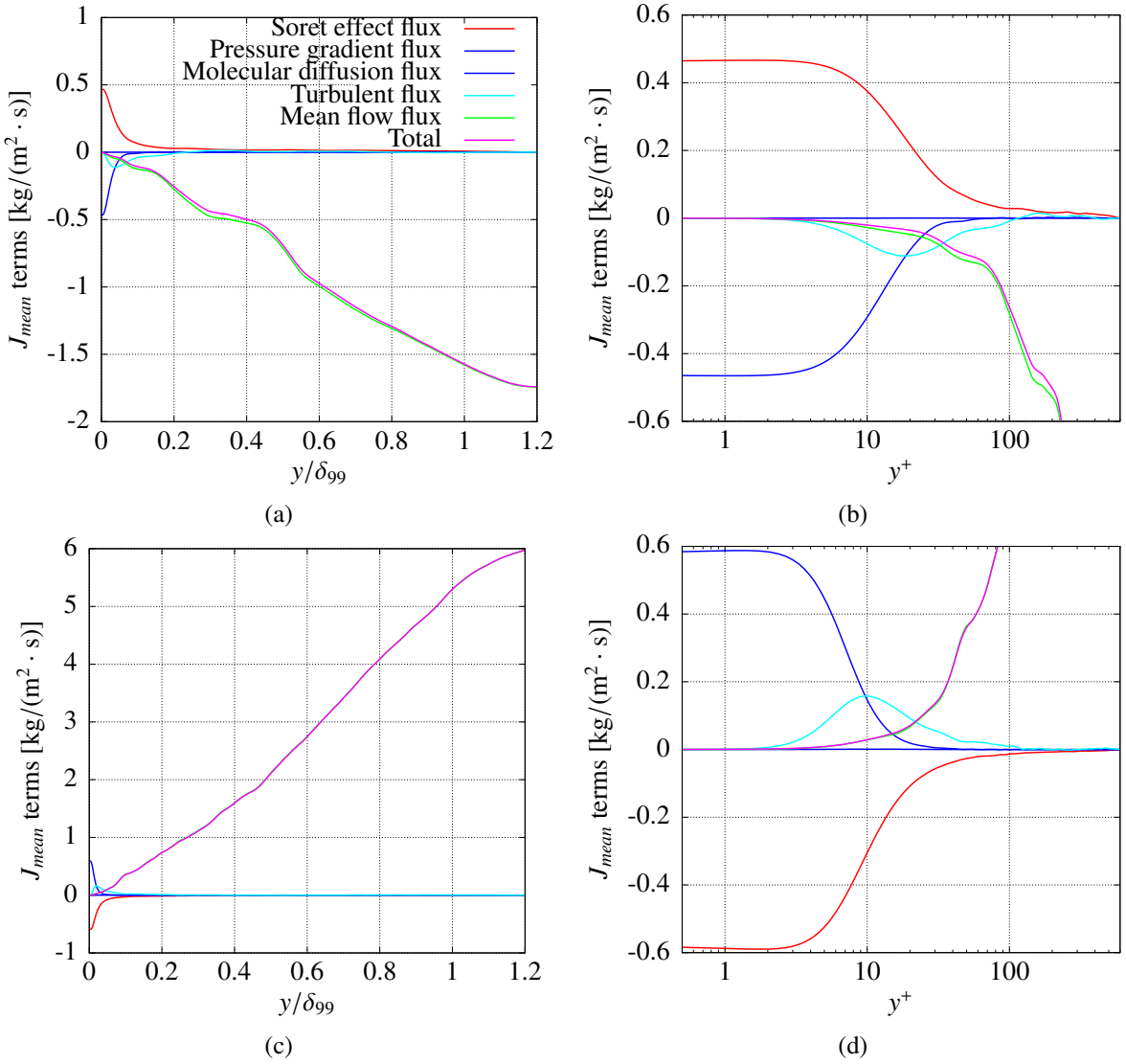

Fig. 6 Species-mass flux of the mean flow field as a function of the outer scaling y/δ_{99} (a, c) and as a function of the wall unit y^+ (b, d): for cases (a, b) T300-600-CH4-25 and (c, d) T600-300-CH4-25.

the wall temperature is different from that in the far field. The temperature gradient induces the Soret effect flux and its absolute value becomes large near the wall due to the large temperature gradient in the wall vicinity as shown in figure 2. The coefficient $D_{T,\alpha}$ is negative, and the temperature gradient is positive in T300-600-CH4-25 and negative in T600-300-CH4-25. Therefore, for T300-600-CH4-25 the Soret effect flux becomes negative and for T600-300-CH4-25 it becomes positive, as shown in figure 6. Thus, for T300-600-CH4-25 the Soret effect decreases the concentration of methane near the wall, whereas for T600-300-CH4-25 it enriches the fluid with methane near the wall. On the other hand, the mass fraction gradient due to the Soret effect induces molecular diffusion flux in the opposite direction. Since the molecular diffusion flux is proportional to the mass fraction gradient, the molecular diffusion flux becomes significant to balance the Soret effect flux.

VI. Conclusion

Direct Numerical Simulations of binary-species temporal boundary layers at high pressure have been performed to investigate the flow physics when the fluid has initially a uniform composition. The working fluid is a mixture of 25 % methane and 75 % nitrogen in terms of mass fraction. The initial pressure is 60 atm. All statistics are obtained at similar friction Reynolds number with $Re_\tau \approx 500$.

The analysis showed that the mean profile of the mass fraction has a gradient in the wall-normal direction despite the uniform initial composition. The mass fraction gradient becomes steeper near the wall in all cases. Since regular diffusion would never induce a mass fraction gradient in the present configuration, this result indicates that uphill diffusion occurs in the present flow field. The velocity fluctuation profiles showed that the qualitative characteristics of velocity fluctuations in the present binary-species high-pressure boundary layers are similar to those of incompressible constant-property boundary layers. The investigation of fluctuations of the mass fraction revealed that the mass fraction fluctuates in the entire boundary layer, indicating that uphill diffusion occurs even far from the wall.

Investigation of the species-mass diffusion balance for mean flow fields clarified the physics and showed that the Soret effect flux and the molecular diffusion flux become dominant near the wall. The Soret effect flux enriches the fluid with methane near the wall in hotter wall case, whereas it decreases the concentration of methane near the wall in colder wall case. The direction of the Soret effect flux is opposite to the mass diffusion flux and the Soret effect flux causes the mass fraction gradient in the binary-species boundary layers at high-pressure.

Acknowledgments

This study was conducted at the Jet Propulsion Laboratory (JPL) and California Institute of Technology (Caltech) and sponsored at Caltech by the Department of Energy, Basic Energy Sciences under the direction of Dr. Wade Sisk. The computational resources were provided by NASA Advanced Supercomputing at the NASA Ames Research Center.

References

[1] Faith, L. E., Ackerman, G. H., and Henderson, H. T., Heat Sink Capability of Jet A Fuel: Heat Transfer and Coking Studies, S–14115, NASA CR–72951, Shell Development Co., 1971.

[2] Kawai, S., "Heated Transcritical and Unheated Non-transcritical Turbulent Boundary Layers at Supercritical Pressures," *Journal of Fluid Mechanics*, Vol. 865, 2019, pp. 563–601. https://doi.org/10.1017/jfm.2019.13.

[3] Toki, T., and Bellan, J., "Investigation of species-mass diffusion in binary-species boundary layers at high pressure using direct numerical simulations," *Journal of Fluid Mechanics*, Vol. 928, No. A18, 2021. https://doi.org/10.1017/jfm.2021.814.

[4] Bae, J. H., Yoo, J. Y., and Choi, H., "Direct Numerical Simulation of Turbulent Supercritical Flows with Heat Transfer," *Physics of Fluids*, Vol. 17, 105104, 2005. https://doi.org/10.1063/1.2047588.

[5] Bae, J. H., Yoo, J. Y., and McEligot, D. M., "Direct Numerical Simulation of heated CO2 flows at supercritical pressure in a vertical annulus at $Re = 8900$," *Physics of Fluids*, Vol. 20, 055108, 2008. https://doi.org/10.1063/2927488.

[6] Nemati, H., Patel, A., Boersma, B. J., and Pecnik, R., "Mean Statistics of a Heated Turbulent Pipe Flow at Supercritical Pressure," *International Journal of Heat and Mass Transfer*, Vol. 83, 2015, pp. 741–752. https://doi.org/10.1016/j.ijheatmasstransfer.2014.12.039.

[7] Nemati, H., Patel, A., Boersma, B. J., and Pecnik, R., "The effect of thermal boundary conditions on forced convection heat transfer to fluids at supercritical pressure," *Journal of Fluid Mechanics*, Vol. 800, 2016, pp. 531–556. https://doi.org/10.1017/jfm.2016.411.

[8] Peeters, J.W. R., Pecnik, R., Rohde, M., Hagen, T. H. J. J. V. D., and Boersma, B. J., "Turbulence Attenuation in Simultaneously Heated and Cooled Annular Flows at Supercritical Pressure," *Journal of Fluid Mechanics*, Vol. 799, 2016, pp. 505–540. https://doi.org/10.1017/jfm.2016.383.

[9] Ma, P. C., Yang, X. I. A., and Ihme, M., "Structure of Wall-bounded Flows at Transcritical Conditions," *Physical Review Fluids*, Vol. 3, 034609, 2018. https://doi.org/10.1103/PhysRevFluids.3.034609.

[10] Toki, T., Teramoto, S., and Okamoto, K., "Velocity and temperature profiles in turbulent channel flow at supercritical pressure," *Journal of Propulsion and Power*, Vol. 36, 2020, pp. 3–13. https://doi.org/10.2514/1.B37381.

[11] Kim, K., Hickey, J.-P., and Scalo, C., "Pseudophase change effects in turbulent channel flow under transcritical temperature conditions," *Journal of Fluid Mechanics*, Vol. 871, 2019, pp. 52–91. https://doi.org/10.1017/jfm.2019.292.

[12] Okong'o, N. A., and Bellan, J., "Direct numerical simulation of a transitional supercritical binary mixing layer: heptane and nitrogen," *Journal of Fluid Mechanics*, Vol. 464, 2002, pp. 1–34. https://doi.org/10.1017/S0022112002008480.

[13] Harstad, K. G., and Bellan, J., "Mixing rules for multicomponent mixture mass diffusion coefficients and thermal diffusion factors," *Journal of Chemical Physics*, Vol. 120, No. 12, 2004, pp. 5664–5673. https://doi.org/10.1063/1.1650296.

[14] Ern, A., and Giovangigli, V., "Thermal diffusion effects in hydrogen-air and methane-air flames," *Combustion Theory and Modelling*, Vol. 2, 1998, pp. 349–372. https://doi.org/10.1088/1364-7830/2/4/001.

[15] Masi, E., Bellan, J., Harstad, K. G., and Okong'o, N. A., "Multi-species turbulent mixing under supercritical-pressure conditions: modelling direct numerical simulation and analysis revealing species spinodal decomposition," *Journal of Fluid Mechanics*, Vol. 721, 2013, pp. 578–626. https://doi.org/10.1017/jfm.2013.70.

[16] Sciacovelli, L., and Bellan, J., "The influence of the chemical composition representation according to the number of species during mixing in high-pressure turbulent flows," *Journal of Fluid Mechanics*, Vol. 863, 2019, pp. 293–340. https://doi.org/10.1017/jfm.2018.992.

[17] Harstad, K., Miller, R. S., and Bellan, J., "Efficient High-pressure State Equations," *AIChE Journal*, Vol. 43, 1997, pp. 1605–1610. https://doi.org/10.1002/aic.690430624.

[18] Okong'o, N. A., Harstad, K., and Bellan, J., "Direct numerical simulation of O_2/H_2 temporal mixing layers under supercritical conditions," *AIAA Journal*, Vol. 40, 2002, pp. 914–926. https://doi.org/10.2514/2.1728.

[19] Knapp, H., Doring, R., Oellrich, L., Plocker, U., and Prausnitz, J. M., *Vapor-Liquid Equilibria for Mixtures of Low Boiling Substances Vol. 6*, Dechema, 1982.

[20] Lele, S. K., "Compact finite difference schemes with spectral-like resolution," *Journal of Computational Physics*, Vol. 103, 1992, pp. 16–42. https://doi.org/10.1016/0021-9991(92)90324-R.

[21] Gaitonde, D. V., "High-order schemes for Navier-Stokes equations: algorithm and implementation into FDL3DI," Air Force Research Lab Wright-Patterson AFB OH Air Vehicles Directorate AFRL-VA-WP-TR-1998-3060, 1998.

[22] Müller, S. M., and Scheerer, D., "A method to parallelize tridiagonal solvers," *Parallel Computing*, Vol. 17, 1991, pp. 181–188. https://doi.org/10.1016/S0167-8191(05)80104-8.

[23] Kozul, M., Chung, D., and Monty, J. P., "Direct numerical simulation of the incompressible temporally developing turbulent boundary layer," *Journal of Fluid Mechanics*, Vol. 796, 2016, pp. 437–472. https://doi.org/10.1017/jfm.2016.207.

[24] Schlatter, P., and Örlü, R., "Assessment of direct numerical simulation data of turbulent boundary layers," *Journal of Fluid Mechanics*, Vol. 659, 2010, pp. 116–126. https://doi.org/10.1017/S0022112010003113

[25] Duan, L., Beekman, I., and Martin, P. M., "Direct numerical simulation of hypersonic turbulent boundary layers. Part 2. Effect of wall temperature," *Journal of Fluid Mechanics*, Vol. 655, 2010, pp. 419–445. https://doi.org/10.1017/S0022112010000959.

[26] Duan, L., Beekman, I., and Martin, P. M., "Direct numerical simulation of hypersonic turbulent boundary layers. Part 3. Effect of Mach number," *Journal of Fluid Mechanics*, Vol. 672, 2010, pp. 245–267. https://doi.org/10.1017/S0022112010005902.

[27] Zonta, F., Marchioli, C., and Soldati, A., "Modulation of turbulence in forced convection by temperature-dependent viscosity," *Journal of Fluid Mechanics*, Vol. 697, 2012, pp. 150–174. https://doi.org/10.1017/jfm.2012.67.

[28] Lee, J., Jung, S. Y., Sung, H. J., and Zaki, T. A., "Effect of wall heating on turbulent boundary layers with temperature-dependent viscosity," *Journal of Fluid Mechanics*, Vol. 726, 2013, pp. 196–225. https://doi.org/10.1017/jfm.2013.211.

[29] Patel, A., Boersma, B. J., and Pecnik, R., "The influence of near-wall density and viscosity gradients on turbulence in channel flows," *Journal of Fluid Mechanics*, Vol. 809, 2016, pp. 793–820. https://doi.org/10.1017/jfm.2016.689.

[30] Taylor, R., and Krishna, R., *Multicomponent Mass Transfer*, John Wiley & Sons., 1993.